Region-based online flaw detection of 3D printing via fringe projection

Xinyue Zhao[1] , **Qiaolong Lian**[1], **Zaixing He**[1,2] and **Shuyou Zhang**[1]

[1] State Key Lab of Fluid Power & Mechatronic Systems, School of Mechanical Engineering, Zhejiang University, Hangzhou, People's Republic of China

E-mail: zaixinghe@zju.edu.cn

Abstract

Additive manufacturing allows for the production of custom parts with complex internal features. However, a lack of online detection of the printing process is one of the challenges that has prevented further improvements in additive manufacturing. This paper proposes a novel online monitoring technique based on a fringe projector to keep the stability of the process under control on a layer-by-layer basis. To detect microdefects with a magnitude smaller than the noise, we propose a region-based defect detection method that takes each subregion, instead of each point, as a detection unit. Compared with a single point, a sub region contains hundreds of points, which represent a domain with greater stability. We combine voxel cloud connectivity segmentation (VCCS) and fast point feature histogram (FPFH) to divide the printing area into hundreds of subregions, smooth the surface to resist the noise based on moving least square (MLS) and evaluate each subregion using local point features. The projection model and normal deviation are developed to extract the sizes and locations of the flaws. The performances of the techniques are demonstrated with some experiments using different 3D printing objects, which indicate that the proposed method is able to detect various flaws and its detection accuracy is higher than the noise magnitude.

Keywords: online flaw monitor, automated defect detection, point cloud process

(Some figures may appear in colour only in the online journal)

1. Introduction

In recent years, Additive Manufacturing (AM) has attracted increasing attention for industrial applications. Additively produced parts exhibit innovative shapes, complex features and lightweight structures that are difficult or even impossible to produce with conventional processes [1]. However, these advantages come with a possible cost: internal defects due to printing error and residual and thermal stresses. Despite significant technological advances, the defect ratios are still too high with respect to conventional production systems. To solve these problems, online sensing and process monitoring are needed to determine the quality and stability of the process during the layer-wise production of the part.

Traditionally, online flaw detection techniques of 3D printing include infrared melt pool monitoring, ultrasonic monitoring systems, and strains and residual stress measurement. Infrared melt pool monitoring [2] detects the size and temperature profile of the molten pool during the process of printing to judge whether there were defects based off experience. Infrared methods [3] monitor radiation given off by the melt pool formation during the powder bed fusion (PBF) process, and predict the occurrence of the defects through the size, shape and temperature of the melt pool. Kanko *et al* [4] monitored the melt pool morphology based on a low-coherence interferometric imaging technique, which allows for high-speed, micron-scale, morphology measurements that are robust to interference from the processing laser light. Ultrasonic monitoring system [5] have been integrated into EOS technology machine to record the ultrasonic signals generating longitudinal waves and evaluate the frequency

[2] Author to whom any correspondence should be addressed.

behaviour on successive layer build-ups using a fast-Fourier-transformation. The proposed approach provides qualitative in-process information regarding residual stresses and part porosity. In addition, the use of strain gages mounted on the build platform measure the strains and residual stress in the metal components [6]. The strain changes in a build platform can be measured when SLS-induced layers are successively milled off. Kleszczynski *et al* [7] investigated the use of an accelerometer mounted in the recoating system to measure its vibration during the printing process. They [8] combined the acceleration measurements and image-based edge analysis for the detection of super elevated edges and possible recoater wear. Patatri *et al* [9] placed two coplanar electrical contacts on the exterior surface of the structure. The capacitance decreases as the number of defects increases. In addition, capacitance measurement has been used for sensing the stress in a 3D-printed polymer structure [10].

The above techniques predict the occurrence of the defects by monitoring the physical attributes of the 3D printing process, which determine the quality and stability of the process. However, these methods use indirect methods of monitoring the printing process, and their accuracy is relatively low.

In recent years, the use of machine vision to directly monitor defects in the 3D printing process has begun to increase [11]. These machine vision approaches are primarily based on 2D vision. In early studies, several attempts to use monocular cameras for two-dimension geometric measurements and defect detection were made [12]. Kruth *et al* [13] used a combination of a visual inspection camera system and a melt pool monitoring system. They then took advantage of the inspection camera system to inspect the deposition of the powder. Pioter [14] proposed a novel real-time 3D temperature mapping method, which can be applied to active thermography analyses. Straub [15] proposed a method for assessing the quality of 3D print during production, utilizing five cameras. The main idea of the method assumes comparisons of the in-process object to the model of the final object using the pixel-by-pixel method. Okarma *et al* [16] assumed that the assessment should not be based on the comparison with a reference image. They proposed an approach for the no-reference quality assessment of 3D prints based on the analysis of the gray-level co-occurrence matrix (GLCM) and the chosen Haralick features. Later, some studies considered the categorization of potential error sources [17] and verification of the deposited powder and fusion layers [18].

The above studies demonstrate that online 2D geometric signatures monitoring improves the process's robustness, stability and repeatability and characterizes the geometry of the internal part [19]. However, online monitoring methods working with 2D images are susceptible to ambient light and printing material color, whose robustness is relatively poor.

Recently, there have been a few 3D vision sensing methods for geometric measurements and defect detection during the AM process [20]. Holzmond [21] exhibited the use of a 3D digital image correlation (3D-DIC) system as an online measurement technique to monitor the surface geometry of a print part. The quality assurance system based on fused filament fabrication (FFF) requires adding a layer of paint between each printed layer, or using specific material for printing, since it is impossible to add an additional step to the print process or use fixed materials. Villarraga [22] scanned the printing parts using an XCT machine and created a 3D model. This 3D model was compared with the standard CAD model for discrepancies. However, XCT exhibits a set of challenges [23, 24] such as its relatively slow speed and high costs compared to other measurement techniques. Zhang [25] presented an online surface topography of laser powder bed fusion using fringe projection. They demonstrate that the technique is able to measure surface topography of the powder bed layers during fabrication. Li [26] presented an enhanced phase measuring profilometry (EPMP) to monitor 3D surface topography and 3D contour data of the fusion area.

Although 3D vision sensing methods acquire large amounts of data and quickly detect the onset of defects and process errors [27], they have their own problems. These approaches only categorize the detection piece based on deviations from their respective nominal CAD model, which can only detect large defects and have poor robustness for noise data. Therefore, it is difficult to apply this to the actual production.

In this work, an online flaw detection method in the AM process is proposed based on a fringe projector. Outliers are abnormal points that have significant differences in 3D local features between corresponding model points. 3D local features are characterized by two evaluations indexes, namely FPFH feature [28] and the deviation of the coordinates and normal vector, which accurately describe the topography around the point. Even for printing parts with complex shapes, normal points representing the printed part will not be considered as outliers. After analyzing the outliers extracted from the defect point cloud and the defect-free point cloud, we found that the defect point cloud has the characteristic of aggregation. Disperse outliers may be caused by noise, while clustered outliers are more likely to be defects. Therefore, different from the existing methods, a region-based defect detection method is proposed. The preprocessing surface is divided into hundreds of subregions, and each small subregion contains dozens of 3D points. Each subregion, instead of each point, is detected as a basic unit, because a single point is susceptible to environmental factors and measurement errors, while a subregion containing hundreds of points represents a domain with greater stability.

The main contributions of the research reported are two-folded:

1. A novel region-based defect detection approach is proposed to improve detection accuracy for 3D data with noise. Existing methods independently determine whether each pixel is a defect point based on its depth deviation. Different from the existing methods, our method determines whether it is a defect by analyzing each subregion based on the idea that the outliers representing defects are clustered, while outliers representing noise are dispersed.

2. Practical algorithms are presented to implement the proposed region-based defect detection approach. Specifically, we proposed using the region segmentation algorithm, voxel cloud connectivity segmentation

Table 1. The specifications of the camera and digital light projector.

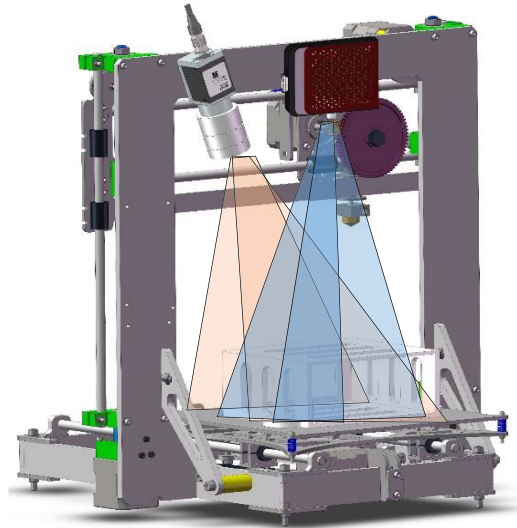| Device	Specifications
Camera	FLIR FL3-U3-13E4M
Image resolution	1280 × 1024 pixels
Lenses	HIK MVL-HF0628M-6MP
Focal length	12 mm
Digital light projector (DLP)	DLP LightCrafter 4500
DLP resolution	912 × 1140 pixels
Software	Visual C+++PCL 1.8

(VCCS), to divide the detection area into hundreds of subregions based on 3D coordinates and geometric features, as well as the fast point feature histogram (FPFH) feature to describe each subregion for detection.

The remainder of this paper is organized as follows. The next section (section 2) introduces the online printing detection system including the print setup and model point preparation. Section 3 presents the preprocessing to remove measurement errors and outliers and smooth surface for the scene data. Section 4 divides the surface into subregions and uses two evaluation indexes to detect and extract the defects.

2. Online printing detection system

To monitor the surface topography of the printing object, once the process of printing each layer is completed, the digital light projector (DLP LightCrafter 4500) will project a series of sinusoidal fringe images onto the printing area. A complementary metal-oxide semiconductor (CMOS) camera (FLIR FL3-U3-13E4M) will be used to capture the fringe images synchronously. The specifications of the camera and the projector are represented in the table 1. The setup of the camera is configured to ensure the largest depth of the field in order to uniform the point cloud density and capture the maximum number of layers in focus. Generally, the point cloud density decreases with the distance from the camera. It is ensured that the camera is perpendicular to the print area to the greatest extent possible. The aperture is stopped down as low as possible while still being able to discern the gray and white squares on the calibration board and all sources of glare is minimized. We keep the projection area in focus and lock the aperture and focus. Also, the camera and projector should be separated by 20 to 45° angle, as formed by the printing parts being scanned. A schematic representing a characteristic online 3D monitoring of geometric signatures in the fused deposition modeling (FDM) process is shown in figure 1. This configuration provides the most illumination.

In this paper, the point cloud acquisition system takes advantage of structured light to achieve 3D photography of objects by manipulating lighting conditions. 3D printing part in view of both the camera and the projector will cause different rays from the camera and projector to intersect one another. This intersection can be calculated using phase-shifted ray information from the projector along with the detected ray information from the captured images. Figure 2

Figure 1. Schematic diagram for online monitoring of geometric signatures in the FDM process.

shows three photographs of objects under different phases, and the decoded point cloud.

In this paper, the printing parts are produced using a FDM type 3D printer (KCMEL 18 pro). FDM type printers are widely used for their low cost, high availability, and ease of modification. We use polylactic acid (PLA) as the printing material, which is fed into a heated nozzle that extrudes filament onto a plate-form or previously deposited filament. The parts are printed layer-by-layer, starting from the bottom layer and finishing on the top [29]. Additively produced parts exhibit innovative shapes, complex features and lightweight structures that are difficult or even impossible to produce using conventional processes. However, these advantages come with a possible cost: internal defects due to printing error and residual and thermal stress [30]. Therefore, developing a novel online monitoring technique is vital in order to keep the stability of the process under control on a layer-by-layer basis.

To detect microflaws from 3D printing parts, it is very important to obtain an accurate and dense standard CAD point cloud in advance for comparison with the extracted structural-light point cloud. We convert the G-code file which is sliced by Cura 14.01 to a.pcd file using a slightly modified open source program gcode2pcd. We can simulate the print line according to the information from the print file and sample to produce a point cloud using the visualization toolkit (VTK) open source library. Each layer of the point cloud can be extracted for detection during the print process. Figure 3 shows that the CAD model (a), simulated CAD point cloud(b), and single slice point cloud (c).

3. Preprocessing

3.1. Outliers removal

Due to the interference of the measurement environment, the surface reflection of the measured workpiece, etc, there are inevitably measurement errors that lead to sparse outliers
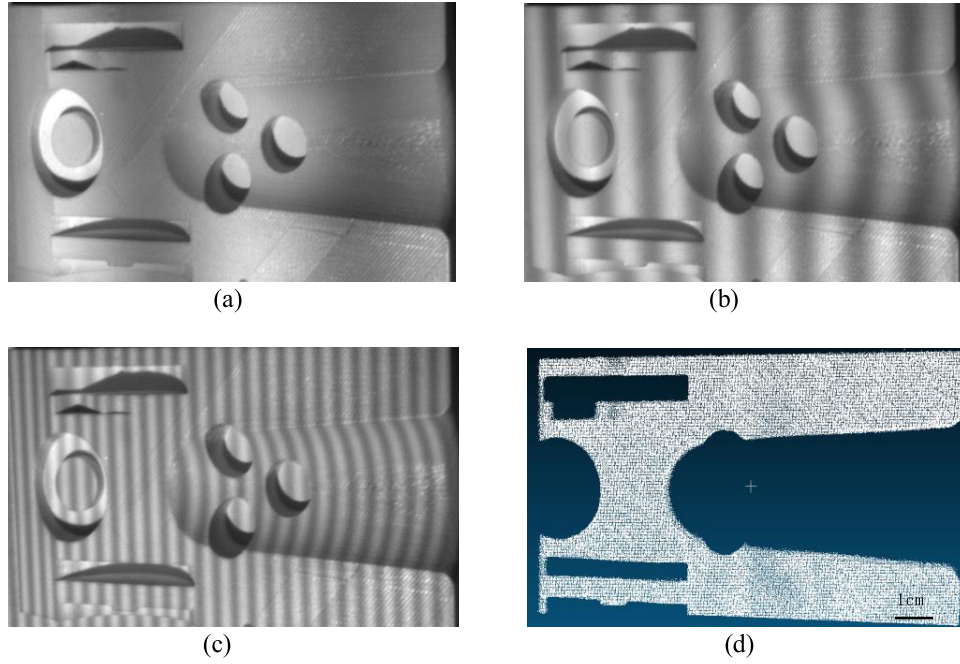
Figure 2. Generation of the point cloud (a)–(c) are three photographs of the objects under different phases, (d) the decoded point cloud.
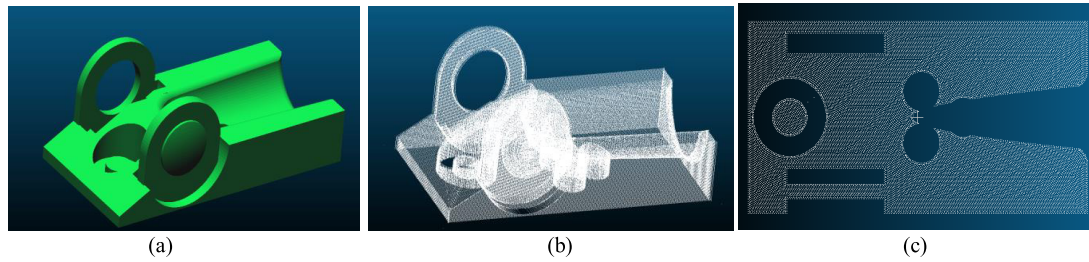

Figure 3. CAD point cloud (a) the CAD model, (b) the simulated CAD point cloud, and (c) the single slice point cloud.

which may corrupt the results. The algorithm mainly employs following steps to remove and correct the outliers.

Step 1: Remove the points of no interest and outliers generated by ambient light interference. Since the region of interest is the top layer of printing, the removal of the point cloud in the nontop layer region can significantly improve the efficiency of subsequent algorithms. Since the print area is known, the maximum and minimum distance is set as the distance threshold to determine whether a point belongs to the detection area.

Step 2: Remove the outliers caused by objects reflecting light. This type of outliers can be solved by performing a statistical analysis on each point's neighborhood. First, for a point (p_i) of the point cloud, count the nearest k points ($p_{i1}, p_{i2...}, p_{ik}$) of point p_i and compute the mean distance from it to all its neighbors. The mean distance of the K-nearest neighbor points of the point p_i is calculated as $d\text{mean}_i = \sum_{j=0}^{k} dij/k$. It is assumed that the resulting distribution is Gaussian with a mean distance and a standard deviation. The mean distance is calculated as $\text{dist} = \sum_{i=0}^{\text{Num}} d\text{Mean}_i/\text{Num}$, and the standard deviation is calculated as $\sigma = \sqrt{\frac{1}{\text{Num}} \sum_{i=1}^{\text{Num}} (\text{dist} - d\text{Mean}_i)}$. Num

is the number of the point cloud in the detection area. All points whose mean distances are outside the interval $[\text{dist} - 3\sigma, \text{dist} + 3\sigma]$ can be considered as outliers and trimmed from the dataset.

3.2. Top layer segmentation

To compare the point cloud with the model file, the top layer is assumed to be planar (Z coordinate value remains unchanged in the same layer printing process), and the top layer point cloud is fit to a plane. The plane fit was performed using Random Sample Consensus (RANSAC) which works under the assumption that the data contains inliers (data can be adjusted to the model) and outliers (data that does not fit the model). The algorithm is nondeterministic: every iteration, the accuracy of the result improves. The process of the algorithm is as follow:

   I Select points at random equal to the minimum number of points required for the given model.
  II Solve the plane coefficient according to the selected points.
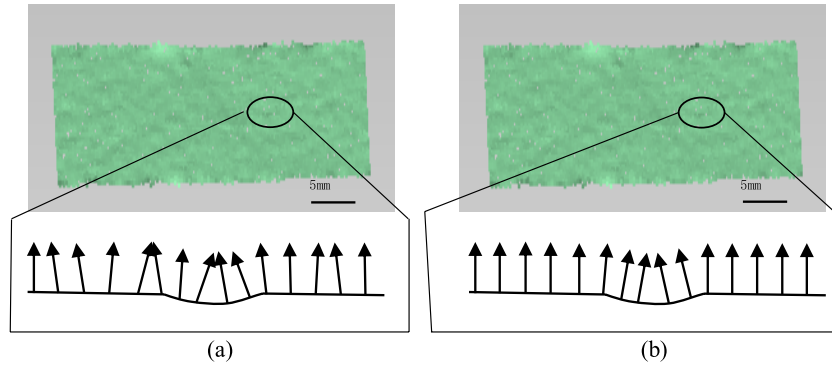 III Determine the number of the points in the tolerance threshold range conform to the plane model.

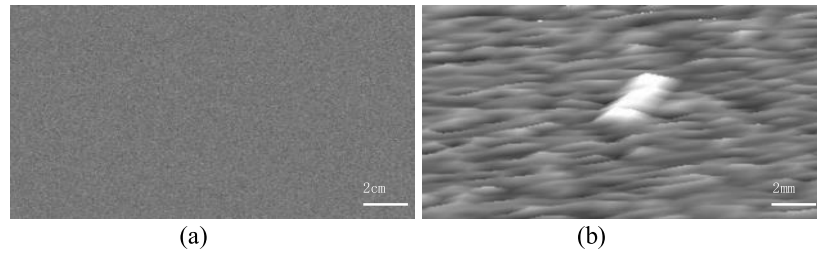**Figure 4.** Surface normal estimation (a) original point cloud using PCA, and (b) smoothed point cloud using MLS.

Figure 5. A planar point cloud with a microflaw: (a) initial view of the flaw, (b) zoomed view of flaw.
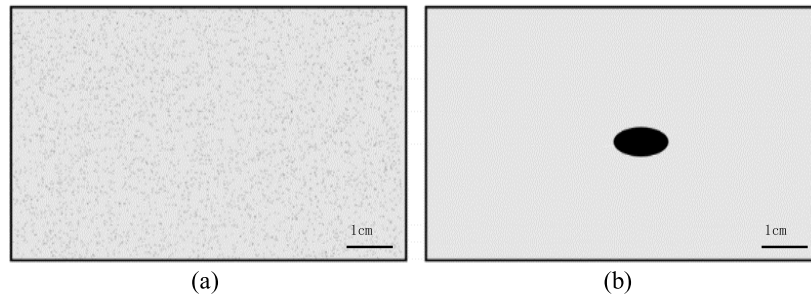

Figure 6. A planar point cloud has data that falls outside tolerance limits due to (a) noise data and (b) the existence of a flaw.

IV If the number of the points is within a specified threshold recalculate the coefficients of the plane, otherwise terminate the algorithm.

V Repeat steps 1–4 until either the maximum number of iterations is reached, or step 4 terminates the algorithm.

3.3. Surface smoothing based on moving least square (MLS)

It is inevitable that measurement errors and outliers exist in the dataset. Some of the data irregularities (caused by small distance measurement errors) are very hard to remove using statistical analysis. The goal of this step is to correct these small errors and smooth surface. This step is very important because it improves the accuracy of the local information. MLS is a method of reconstructing continuous functions from a set of unorganized point samples by calculating a weighed least squares measure biased towards the region around the point at which the reconstructed value is requested [31]. MLS is useful for reconstructing a surface from a set of points. By applying the MLS algorithm, we can obtain more accurate intrinsic properties of the surface such as the normal and curvature shown in figure 4.

The process of the algorithm is as follows:

I Local reference domain H for the interpolating point p is generated using k-d tree and the anticipated feature size.

II The reference domain H for p is used to compute a local bivariate polynomial approximation to the surface in the neighborhood of p. Consider a function: $R^n \mapsto R$ and a set of points $S = \{p_i, f_i | f_{(p_i)} = f_i\}$ where p_i are points adjacent to point p belonging to R^n and $f_i \in R$. The error function of point p is described as equation (1):

$$f_{\mathrm{MLS}}(p_i) = \sum_i (||f(p_i) - f_i||)^2 \Theta(||p - p_i||). \quad (1)$$

III Compute the coefficients of a polynomial approximation f so that the weighted least squares error is minimized.

$$\hat{f} = \min(f_{\mathrm{MLS}}(x_i)) = \min(||f(x_i) - f_i||)^2 \Theta(||x - x_i||). \quad (2)$$

In equations (1) and (2), the function Θ is a smooth, monotone decreasing function, which is positive throughout the entire space. In this article we use a Gaussian function: $\Theta(d) = e^{\frac{-d^2}{h^2}}$, where h is a fixed parameter reflecting the anticipated spacing between neighboring points.

4. Defect detection process

As a consequence of the high dimensional accuracy requirement of 3D-printing objects, it is vital that the online-detection process demands a corresponding detection accuracy. However, in order to ensure a real-time response and robustness, the measurement accuracy and noise cannot satisfy the detection accuracy of the 3D printing. Traditionally, the approach for detecting the presence of the abnormalities (for the Z axis coordinate deviation from the nominal) is not always effective, because the single threshold detection method has limitations that a large detection threshold will bury minor defects, while a small detection threshold will detect excessive pseudo-defects.

For example, consider the 3D data (represented as a point cloud of deviations from a nominal CAD geometry) shown in figure 5(a), where a surface flaw appears in the bottom left corner. The zoomed view of the surface flaw is shown in figure 5(b). There is a microflaw that cannot be detected directly with a large threshold.

In contrary, if a small detection threshold is applied, any data point exceeding the tolerance limit cannot be identified as noise or a defect. For instance, consider two simulated point clouds given in figure 6, where any point greater than the threshold is displayed as black and any point below the threshold is displayed as white. Figure 6(a) is actually a flawless surface while there are several black points caused by noise in the image. Figure 6(b) is a surface with defects, so obviously there are black points due to defects in the image. Therefore, we cannot identify whether a surface is flawless or not based just on the test results.

To accurately detect the microflaw whose magnitude is smaller than noise, we came up with a theory that the convergence of abnormal points may be caused by defects, while disperse abnormal points are more likely to be caused by noise. Therefore, based on the above theory, a region-based evaluation approach is presented, which applies regional division of the detection area, and detects the subregion separately. We regard each subregion instead of each point as a detection unit, and the number of abnormal points within the subregion as an evaluation for potential defect-region extraction. A single point is susceptible to environmental factors and measurement errors, while a subregion containing hundreds of points represents a domain with greater stability. Also, the local 3D surface descriptor FPFH is applied to describe the local topography, which simultaneously improves the detection speed and accuracy.

4.1. VCCS-based potential defect-region division

In this paper, the detection area point cloud is divided into hundreds of subregions, where each subregion contains dozens of points that represent a set of the detection domain. Since region-based detection has a higher detection stability than direct detection (coordinate deviation method), segmentation algorithms aim to group points in the detection scene into perceptually meaningful regions that conform to the surface of the object to be detected. Recently, unsupervised segmentation has been widely researched in point cloud processing. Region-growing algorithms take advantage of the normal vector and curvature to realize segmentation, which is unable to resist noise interference. Marjov random field (MRF) merge relational low-level context within image with object level class knowledge, which have drawback that computational cost rises sharply with increasing number of nodes. Plane Model Segmentation is based on RANSAC plane fitting, which cannot block adjacent points with different features.

We apply a novel method, VCCS [32], which takes advantages of the 3D geometry provided by structure-light point cloud to generate superclusters that conform to the surface of the object to be detected. VCCS is able to cluster adjacent points with similar local low-level features into one subregion, while assuring a regular distribution of the subregions. In addition, it keeps the speed comparable to state-of-the-art methods.

This is accomplished using a seeding methodology based on 3D space and a flow-constrained local iterative clustering which uses 3D coordinates and geometric features. Adjacency is a key element for the VCCS, as it clusters neighboring points with similar local feature. In this work, we transform the point cloud into voxelized 3D space with a given resolution R_{voxel}. All points in the voxel are represented by the center of the voxel's interior point cloud. The adjacency graph is constructed for the voxel cloud by searching the voxel kd-tree. To select a set of seed points, we divide the space into a voxel grid at a given size R_{seed}, which is significantly larger than R_{voxel}. The voxels closest to the center of each grid are selected as the initial seed points. Based on the selected seed points, we take advantage of the adjacency graph by searching for voxel that has the smallest gradient.

We adopt the following notion to represent the voxel at index i within the voxel cloud V of voxel resolution r:

$$V_r(i) = F_{1\ldots n}, \tag{3}$$

where F contains a feature vector that includes n point features (location, normals).

The gradient is calculated in equation (4):

$$G(i) = \sum_{k \in V_{\text{adj}}} \frac{||V(i) - V(k)||}{N_{\text{adj}}}. \tag{4}$$

V_{adj} represents the adjacent voxels of the seed point, and N_{adj} is the number of the adjacent voxels.
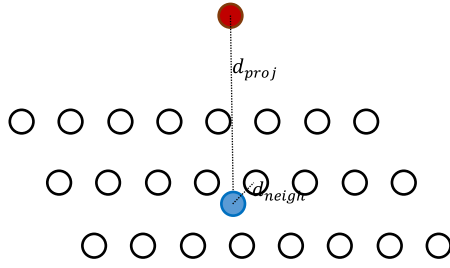
Figure 7. Schematic diagram of the projection model: the red point is the scene point, the blue point is the projection point, and the black points are the model points.

VCCS voxels are clustered by a 7D space, and given in the following notion:

$$F = [x, \ y, z, x_{\text{norm}}, y_{\text{norm}}, z_{\text{norm}}, \text{curvature}] \quad (5)$$

where x, y, z are 3D coordinates, and $x_{\text{norm}}, y_{\text{norm}}, z_{\text{norm}}$, curvature are surface normal information. To calculate the distances in feature space, we normalize our spatial distance D_s with the longest distant of the adjacent voxel that is $\sqrt{3}R_{\text{seed}}$. The normal distance D_n is the Euclidean distance in normal vector space. This leads us to equation (6) for the normalized distance D:

$$D = \sqrt{\frac{w_s D_s^2}{3R_{\text{seed}}^2} + w_n D_n^2} \quad (6)$$

where w_s, w_n control the weight of the space distance, and normal similarity respectively.

The algorithm adopts the iterative method assigning voxels to clusters. First, we select the voxel closest to the cluster center, and grow outward from it to adjacent voxels. The feature space distance from each of these to the seed point defined in equation (6) are calculated. If the distance is the smallest, the cluster will absorb it and assign a fixed label. We add its neighbor that is further from the seed to the search queue for this label using the adjacency graph. To ensure each cluster grows at the same time, one seed absorbs a new voxel at a time, and the next seed is processed. Clusters will process iteratively outwards until it reaching the edge of the search queue.

After the search for all cluster adjacency graphs has finished, we update the centers of each cluster by calculating the mean of all its constituents. As clusters tend to stabilize after a few iterations, we simplify the process with four iterations in this paper.

4.2. FPFH-based defect extraction

The defects of the divided supervoxels are identified by two new evaluation indexes of FPFH based on local points feature and the deviation of the coordinates and normal vector.

FPFH, a local geometrical feature, are pose-invariant features that describe the local surface model properties of points using combinations of their k-nearest points. If the local surface is not flat, FPFH feature represents the plane model feature differently. If the difference is larger than a threshold, the supervoxels are considered to be in a potentially bad area.

The calculation of FPFH is as follows. To begin with, for each point p, all of p's neighbors enclosed in the sphere with a given radius r are extracted (k neighborhood). For each query point p_i we compute the relationships between the point itself and its neighbors. We define a Darboux *uvn* frame for every pair of points p_i and p_j (j is the index of the neighbor points) and their estimated normal n_i and n_j, $u = n_i$, $v = (p_j - p_i) \times u$, $w = u \times v$. The features indicating the differences between the two local topographies are described in equations (7)–(9). We compute the angular variation of n_i and n_j and call this the SPFH.

$$\alpha = v \cdot n_j \quad (7)$$

$$\varphi = (u \cdot (p_j - p_i)) / \|p_j - p_i\| \quad (8)$$

$$\theta = c \arctan(w \cdot n_j, u \cdot n_j). \quad (9)$$

Then, we redetermine its k neighbors and use SPFH values to weight the final histogram of p as FPFH.

$$\text{FPFH}(p) = \text{SPFH}(p) + \frac{1}{k}\sum_{i=1}^{k} \frac{1}{w_k} \cdot \text{SPF}(p_k). \quad (10)$$

Where the weight w_k represents the distance between the query p_i and the neighbor point p_k, which decreases as the distance increases.

Since defects are characterized by the deviation between the scene and the model, the deviation of the coordinates and normal vector are used as the second evaluation. Firstly, scene points are projected onto the model plane, two types Euclidean distances are calculated as the projection distance d_{proj} (distance from the scene point to the projection plane) and neighbor distance d_{neigh} (distance from the projection point to the nearest neighbor in the model). The model diagram is shown in figure 7.

Also, the normal and curvature calculated by MLS are compared with the model, defined as d_{norm} and d_{curv} where w_p, w_n and w_c control the influence of the deviation in the projection distance, normal and curvature respectively, and r is the resolution of the model point cloud.

$$D_{\text{dim}} = \begin{cases} w_p \cdot d_{\text{proj}} + w_n \cdot d_{\text{norm}} + w_c \cdot d_{\text{curv}}, & d_{\text{neigh}} < r \\ \text{fixed great number}, & d_{\text{neigh}} > r \end{cases}. \quad (11)$$

The quality of the divided multiple subregions are evaluated based on the FPFH feature and the deviation of the coordinates and normal vector. Detection quality of the detection area is combined by every subregion. The FPFH features of the subregion are regarded as the criteria for determining whether the surface topography of the corresponding subregions is similar with the model surface.

To represent the distance between the model feature and the corresponding subregion feature, we use the Histogram Intersection Kernel:

$$d\left(\text{FPFH}_{\mu 1}, \text{FPFH}_{\mu 2}\right) = \sum_{i=1}^{nr_{\text{bins}}} \min\left(\text{FPFH}_{\mu_1}^i, \text{FPFH}_{\mu_2}^i\right). \quad (12)$$
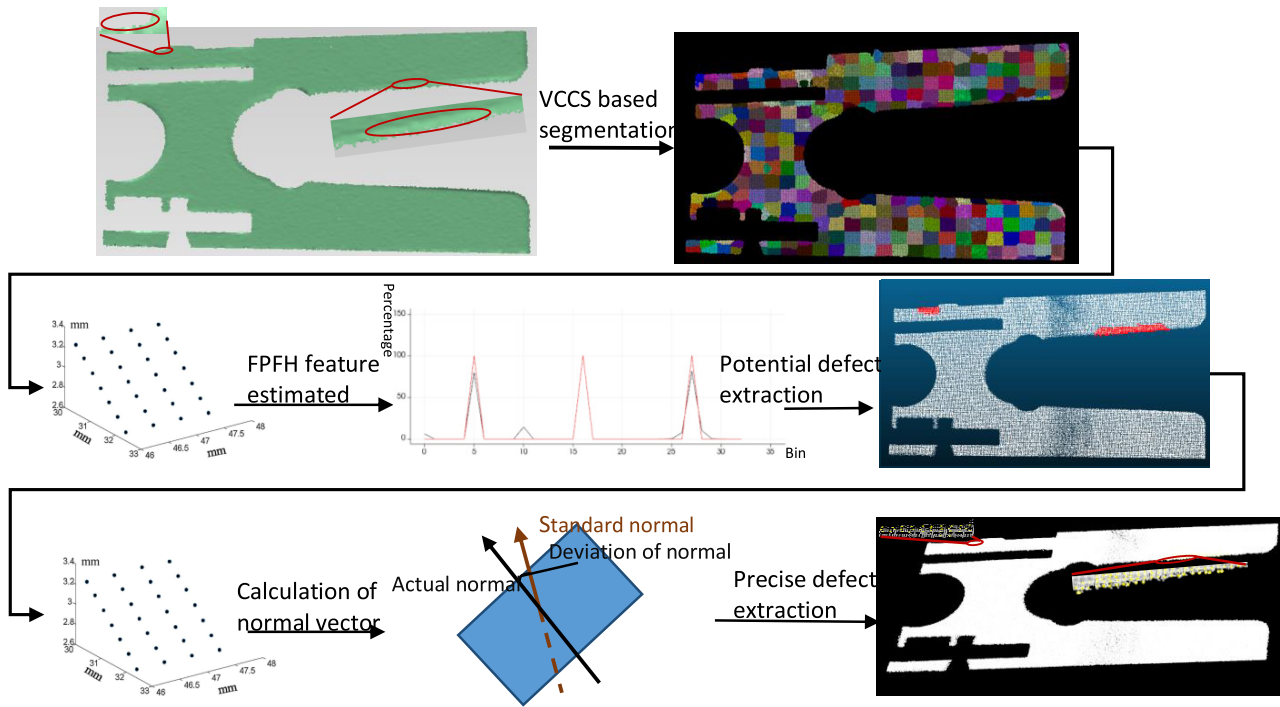
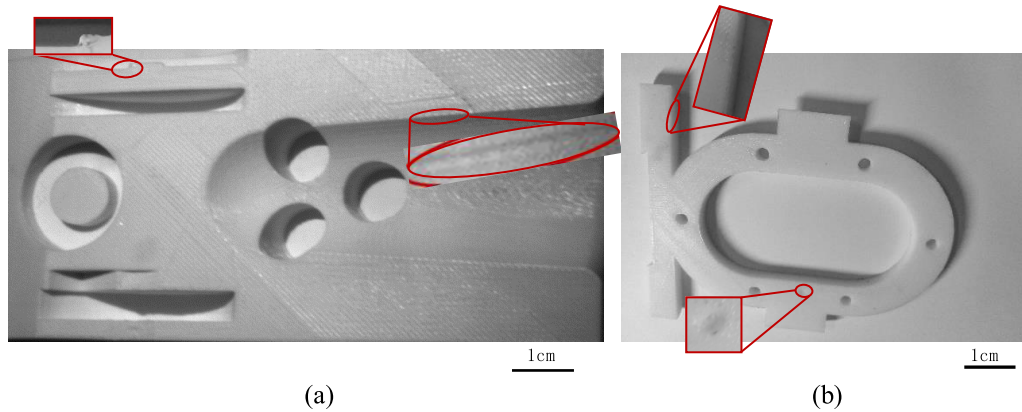**Figure 8.** Calculation of FPFH feature and deviation of normal vector.

Figure 9. Examples from the database in: (a) curling defects on printing medical instruments (size: $7\,\text{mm} \times 0.9\,\text{mm} \times 0.7\,\text{mm}$, $3\,\text{mm} \times 0.6\,\text{mm} \times 0.3\,\text{mm}$), (b) hole defects (size: $3\,\text{mm} \times 2.5\,\text{mm} \times 0.4\,\text{mm}$) which are designed on the CAD model and a curling defect (size: $6\,\text{mm} \times 1.5\,\text{mm} \times 0.4\,\text{mm}$).

If the distance between two features is larger than the threshold, the subregion of the detection area is considered to be a potential defect region. Similarly, the distance D_{dim} based on the deviation of the coordinate and normal vector directly represents the actual difference between the model and scene. The potential defect regions are calculated using D_{dim} criteria. In most situations, the defects are contained in the subregion, which have relatively obvious differences from the model. The calculation of the FPFH feature and the deviation of the normal vector are shown in figure 8.

5. Experiments

To verify the accuracy and effectiveness of the proposed online flaw detection system of the FDM process, experiments are conducted with different types of defects including holes,

bumps, and curling. In these experiments, defects in the real printing process and artificial design defects are detected.

Measurement resolution is directly related to the density and accuracy of the point cloud. The density of the point cloud depends on the resolution of the projector (generally the camera resolution is much higher than that of the projector) and the size of the projection area. In this paper, the point cloud acquisition system uses devices that include a projector DLP Lightcrafter 4500, and a CMOS camera FLIR FL3-U3-13E4M, which can acquire approximately 2000 points cm^{-2}, the distance between adjacent points is approximately $0.2\,\text{mm}$.

In order to understand how difficult it is to detect and recognize a microflaw on a printing part, figures 9(a) and (b) represent two examples with defects that can be detected. Figure 9(a) is a picture of a real object from a medical device model, which has two curling defects (size: $7\,\text{mm} \times 0.9\,\text{mm} \times 0.7\,\text{mm}$,
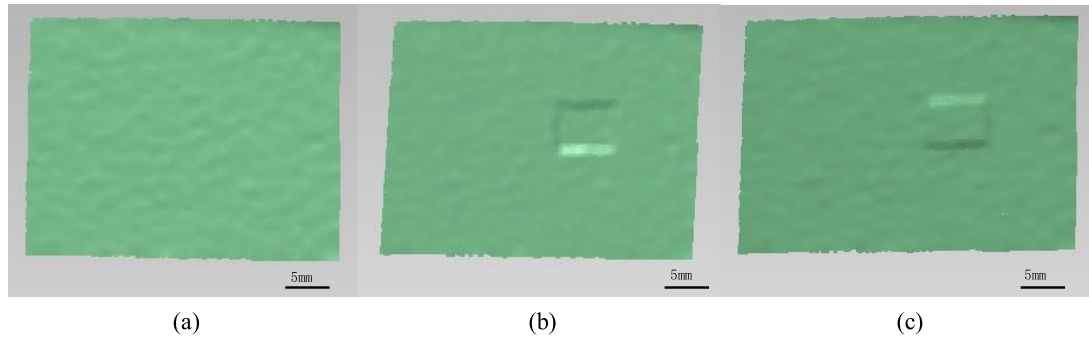
Figure 10. Three different surface topographies created from the same point cloud: (a) plane area without flaw; (b) plane area with a bump; (c) plane area with a hole.
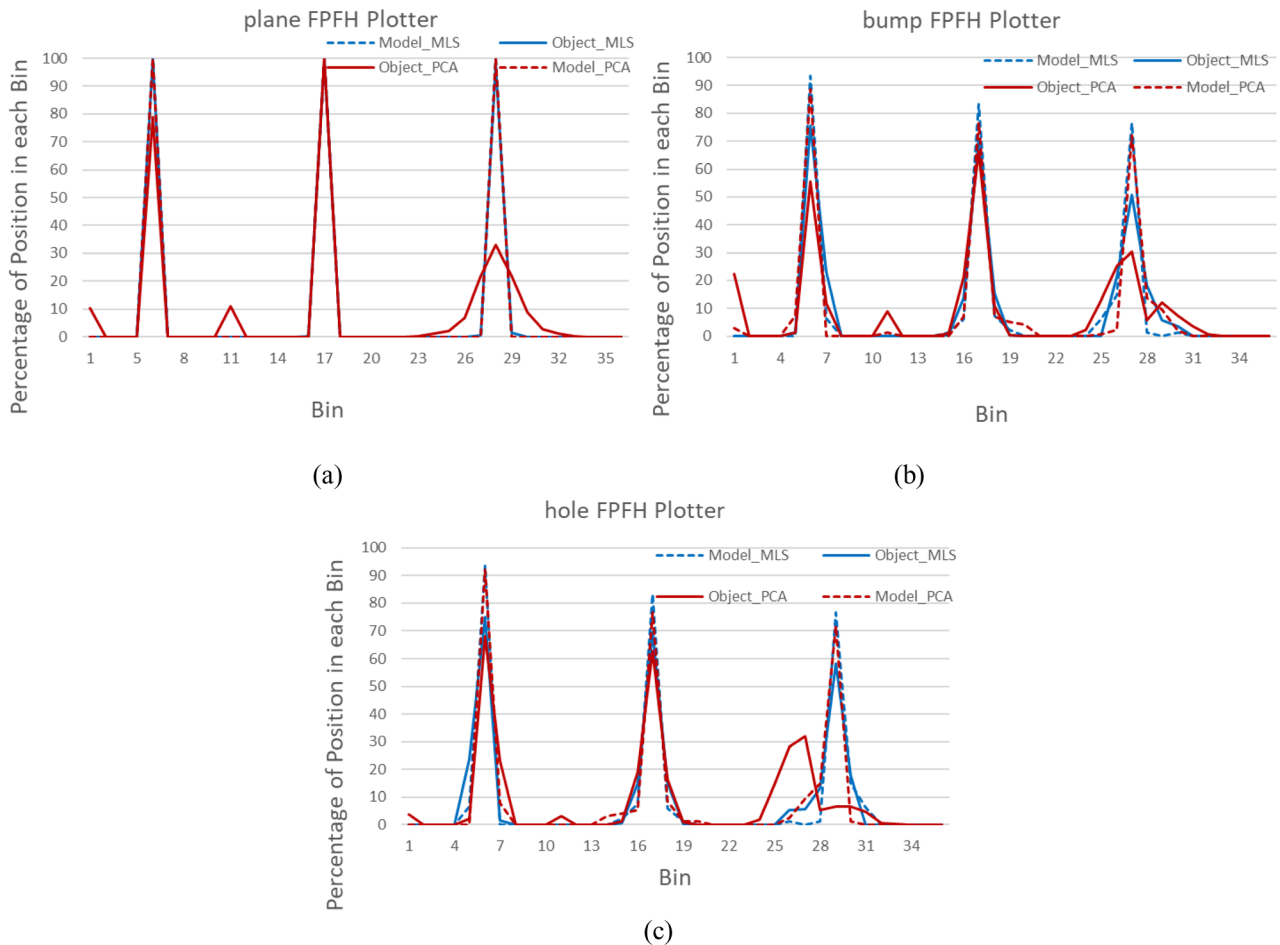

Figure 11. Comparison of the results for calculating FPFH using the MLS versus PCA method, both on the model and object at the same area. (a) Point on the plane area; (b) point on the bump area; (c) point on the hole area.

$3 \, mm \times 0.6 \, mm \times 0.3 \, mm$). Figure 9(b) shows a paddle with a hole (size: $3 \, mm \times 2.5 \, mm \times 0.4 \, mm$) which is designed on the CAD model, and a curling defect (size: $6 \, mm \times 1.5 \, mm \times 0.4 \, mm$). There are corresponding local enlarged views of the defects.

5.1. Evaluation of the FPFH estimation based on MLS

The 3D surface local descriptor FPFH is the evaluation index in the region-based detection which represents the points' local regional feature. The precision of the feature calculation directly influences the results of the detection. In this section, we evaluate how the computation of the FPFH is affected when PCA (principal component analysis) or MLS methodologies are used. (PCA-based FPFH is a traditional method while MLS-based FPFH is a refined method). In order to verify the FPFH accuracy on different surface topography, figures 10(a)–(c) shows three surface topographies with distinctive features: a plane area without flaw, a plane area with a bump (size: $2 \, mm \times 1.5 \, mm \times 0.2 \, mm$), and a plane area with a hole (size: $2 \, mm \times 1.5 \, mm \times 0.2 \, mm$). In addition, the bump and the hole are located in the same area.
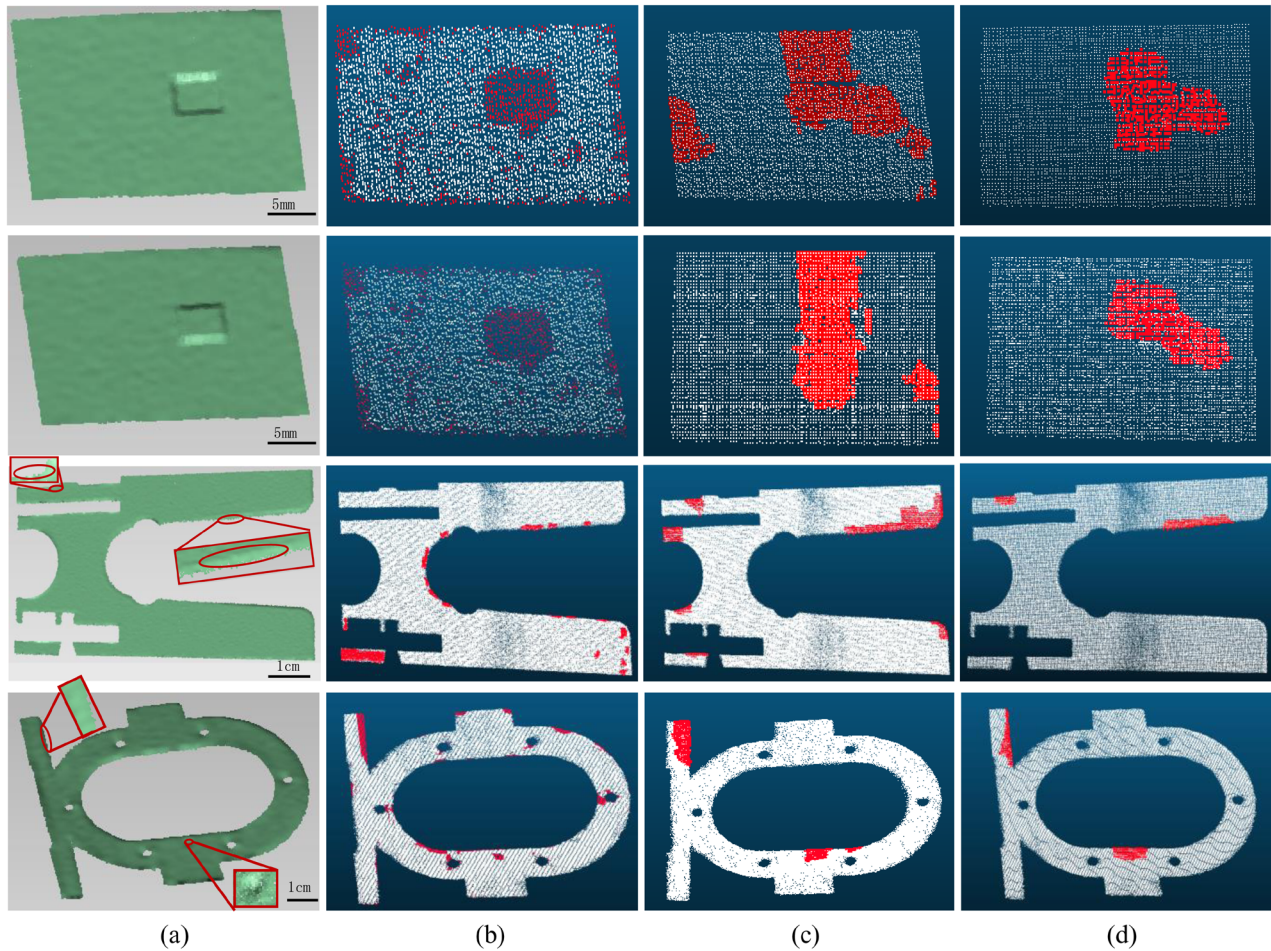
Figure 12. The results of the detection by three methods. (a) Point cloud renderings of four different topographies that contain various defect types; (b) the detection results of the region grow method; (c) the detection results of VCCS and conventional FPFH; (d) the detection results of the proposed method.

In order to evaluate the robustness to noise for calculating the FPFH, in figures 11(a)–(c) we show a comparison between the results of calculating the FPFH using the MLS versus the PCA method both on the model and object at the same area. In addition, the parameters of the two algorithms are set to be the same: taking the data in the range of 1.0 mm into consideration. Figures 11(a)–(c) show that as for model point, the red dotted line and the blue dotted line calculated by two methodologies are almost overlapped, for there is no noise interfering with the result. Although robustness to noise is one of the most important factors to 3D local descriptor, noise can be more or less interfere with the accuracy of the descriptors, especially for dense point clouds. For the object point cloud, there are measurement errors caused by factors, such as noise due to reflecting light, and the measuring accuracy. It is vital to use a methodology that can resist the influence of noise and accurately represent the surface topography.

In figure 11(a), the blue solid line represents FPFH using MLS method which is more consistent with the ground truth than red solid line. Figure 11(b) represents the point on the bump area. Figure 11(c) represents the point on the hole area. FPFH using MLS method is closer to the ground truth. It can be seen that through the proposed method, a better FPFH accuracy in different surface topographies is obtained, especially

in uneven topography. The conventional PCA method directly calculates the normal vector of the points and estimates the local feature. A high-density point cloud arranges compact and can be influenced significantly by small measurement errors. The function of MLS is to correct small errors and smooth surface. This step is very important because it improves the accuracy of the local information. Consequently, FPFH estimated based on MLS will increase the accuracy and effectiveness of the segmentation.

5.2. Evaluation of the potential defect area segmentation

In order to evaluate the detection accuracy of the combination between the VCCS and the refined FPFH, it is compared with the VCCS, the conventional FPFH and the region grow method with different topographies. A combination of the VCCS and FPFH, which is the key step of detection, is vital for overall detection accuracy and efficiency. The regional topography's changes caused by microdefects are too small to be extracted as defects, which lead to leak detection. On the other hand, due to the presence of noise, some normal regions are detected as defect areas not only increase the workload of the fine detection process, but also increase the possibility of false detection.
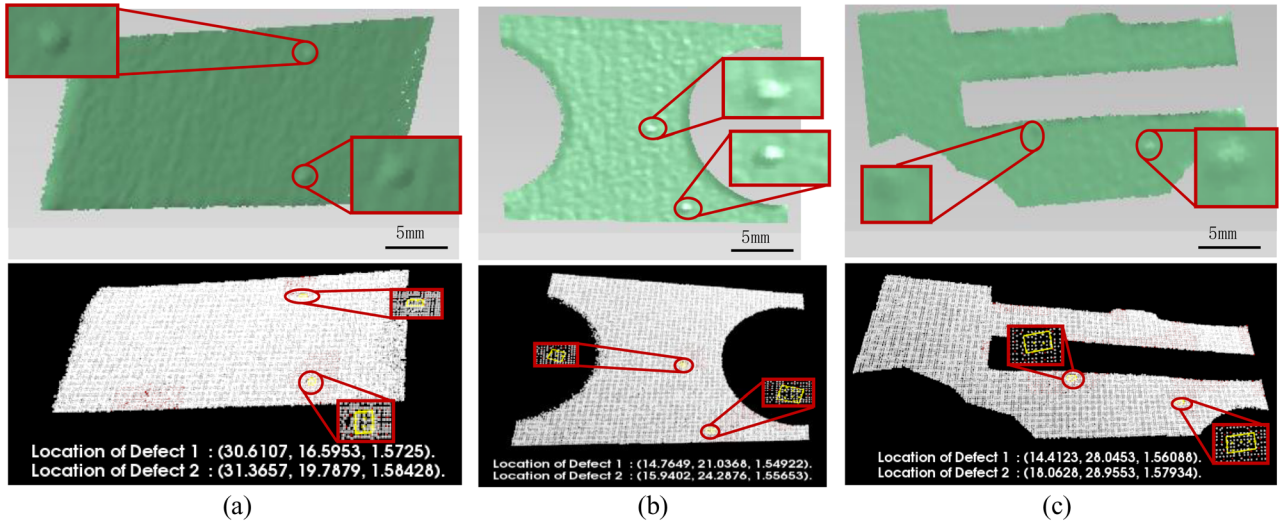
Figure 13. Some examples of detection results based on simulation point cloud. The first line shows the point cloud rendering, the second line shows the results of the defective surface based on the proposed method.
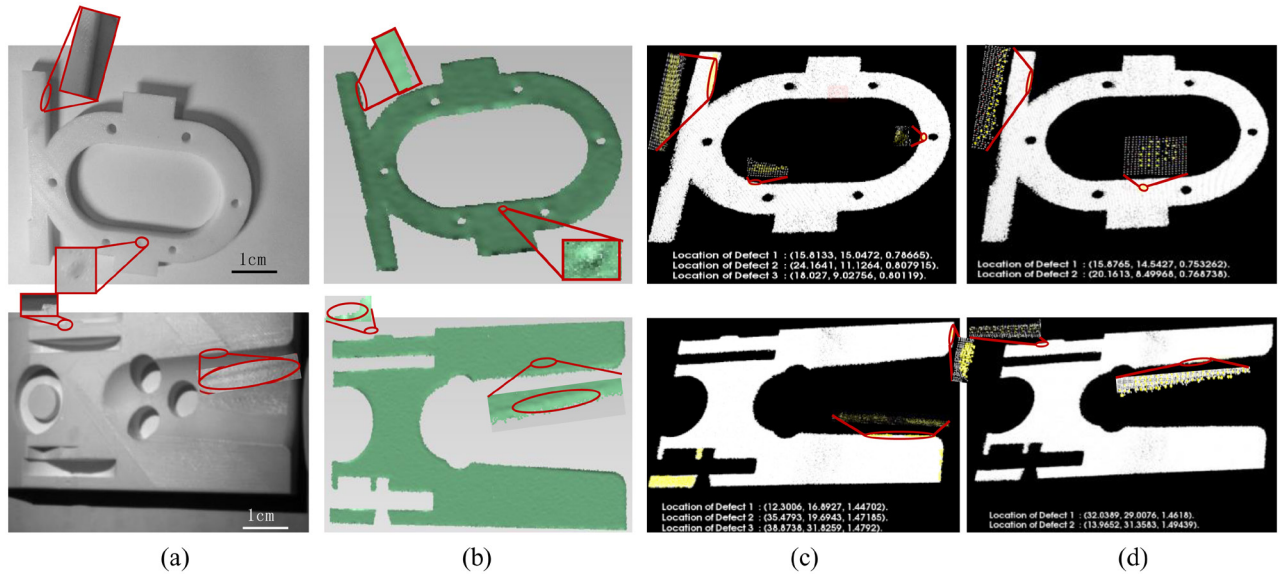

Figure 14. Detection results by two methods. (a) Real picture of the objects to be detected, (b) point cloud rendering of the top layer, (c) detection results by the region grow methods, and (d) detection results by the proposed method.

Figure 12 represents the results of the coarse detection by the three methods. Figure 12(a) shows the point cloud renderings of four different topographies, which contain various defect types (holes, bumps, and curling). Figure 12(b) shows the result of region grow method [33]. Figure 12(c) presents the results by the VCCS and convention FPFH, and figure 12(d) shows the results based on VCCS and refined FPFH. Compared with the last three columns, it is obvious that our method is superior to the other methods. Although traditional methods can detect defect contours more accurately, this does not matter since the fine detection can extract flaws precisely. However, because of the noise it has many scattered false detection. Furthermore, the results by VCCS and conventional FPFH also include false detection and inaccuracy results. The above two methods are, to some extent, affected by the unstable normal vector in the edge region. Consequently, our proposed method has a greater performance.

5.3. 3D surface topography monitoring of the printing part

In order to accurately detect the surface topography of the printing part, there are three different types of data that are essential for characterizing the defects information: (1) the original point cloud, (2) the potential defect point cloud, which has been extracted in section 5.2, and (3) identified points belonging to the flaw.

In this section, the projection model is used to evaluate whether defects exist in each subregion. We synthetically take the projection distance, the difference of the normal vector and curvature into consideration, and extract outliers from potential defect areas. In case of more than one defect, a Euclidean cluster algorithm clusters all outliers to obtain the number of the defects. For each point in a defect region, we estimate the values $\Delta z(p_i) = z_{p(\text{ideal})} - z(p_i)$. The extreme point of the defect is determined by $\max\{|\Delta z(p_i)|\}$ among all points from

the defect region. The sign of $\Delta z(p_i)$ determines if the defect is a bump or a hole. A bump is detected when $\Delta z(p_i)$ is positive and a hole is detected when $\Delta z(p_i)$ is negative.

In order to evaluate the full methodology of online flaw detection proposed in this paper, we randomly generate 0–2 defects at any position on the basis of the existing point cloud with noise. Artificial defects include the following types: holes, bumps, cracks. In addition, all these defects area are less than $6\,mm^2$, and the max depth is less than $0.3\,mm$. Figure 13 shows some examples of the detection results based on the simulation point cloud. The white point is the original point cloud, and the yellow point is identified point belonging to the flaw. Eight yellow lines form the defect bounding box. As shown in figure 13, the proposed online flaw detection method can detect objects with arbitrary shapes. Also, our method can extract the number of defects and locate it.

In order to validate the performance of the proposed approach, the region grow method is used for comparison. In figure 14, (a) is the real picture of the objects to be detected, (b) is the point cloud rendering of the top layer, (c) is the results by the region grow methods, and (d) is the results of the proposed method. Comparing the last two columns, it is obvious that our method is superior to the other ones. We can observe that the size and shape of the defects detected by our method are more consistent with the real defects under the same point cloud density and accuracy conditions. The proposed method can accurately detect microdefects whose area is larger than $6\,mm^2$ and whose height deviation is $0.2\,mm$ based on our point cloud acquisition system. In addition, our methods can resist the error detection caused by edge area and noise.

It is vital for online detection whether single-layer detection speed is greater than the corresponding printing time. Generally, single-layer printing time and detection time increase with an increasing printing area. In this paper, the size of the printing model is approximately $120\,mm \times 60\,mm$. The point cloud process time for each layer is significantly shorter than the printing time. Time of online detection consists of point cloud acquisition and processing, and the corresponding times are 0.83 s and 1.21 s, respectively, for a point cloud with approximately 1 million points. All measurements were conducted on an Intel Core i5 3.4 GHz processor. However, it takes 40 s which is significantly greater than the detection time for each layer printing. Therefore, our method can fully meet the requirements of online detection in terms of speed.

6. Conclusion

In this paper, we presented a novel point cloud idea that the outliers representing defects are clustered while outliers representing noise are discrete, and practical algorithms were presented to implement the proposed region-based defect detection approach. The proposed methodology is divided into two main processes. The first process is subregion segmentation. In this step, the printing part's surface is segmented into hundreds of subregions which represent a set of detection domains. The segmentation algorithm takes advantages of the 3D geometry provided by structure-light point cloud to generate subregions that conform to the surface of the object to be detected. In the next process, we applied two evaluation indexes, namely, FPFH feature and deviation of the coordinates and normal vector to identify defects. Surface smoothing based on MLS and local descriptor FPFH are presented to the extracted potential defect area in coarse detection, and a projection model is used to evaluate whether defects exist in each potential area. Experiments are conducted on real data captured by strcuture light system on the printing parts. The experimental results demonstrate that our approach is scalable, accurate and robust for point cloud with noise and can detect different types of defectd, such as holes, bumps, cracks.

The key findings of the study can be summarized as follows.

(1) Structure light-based 3D vision is effective in real-time direct defect detection in 3D printing. Compared with existing indirect detection methods, such as infrared melt pool monitoring, ultrasonic monitoring systems, strains and residual stress measurement, it is more accurate and reliable.
(2) The aggregation of outliers is an important characteristic of a defect. Noise inevitably exists in the point cloud acquired by the structure light system. However, the noisy outlier points are dispersed, while the defect outlier points are clustered. This important characteristic can help to distinguish a defect from noise.
(3) Dividing the point cloud into hundreds of subregions and extracting its local features for defect detection can greatly improve the detection robustness. Different from traditional methods using a single point as the detect unit, the region segmentation and description steps can utilize the aggregation characteristic of defect outliers, which leads to the accurate detection of the microflaw whose deviation amplitude is even smaller than noise.

ORCID iDs

Xinyue Zhao https://orcid.org/0000-0002-7184-0985
Zaixing He https://orcid.org/0000-0003-0577-8009
Shuyou Zhang https://orcid.org/0000-0001-9023-5361

References

[1] Lanzotti A, Grasso M, Staiano G and Martorelli M 2015 The impact of process parameters on mechanical properties of parts fabricated in PLA with an open-source 3D printer *Rapid Prototyp. J.* **21** 604–17
[2] Berumen S, Bechmann F, Lindner S, Kruth J-P and Craeghs T 2010 Quality control of laser- and powder bed-based

additive manufacturing (AM) technologies *Phys. Procedia* **5** 617–22

[3] Doubenskaia M A, Zhirnov I V, Teleshevskiy V I, Bertrand P and Smurov I Y 2015 Determination of true temperature in selective laser melting of metal powder using infrared camera *Mater. Sci. Forum* **834** 93–102

[4] Kanko J A, Sibley A P and Fraser J M 2016 *In situ* morphologybased defect detection of selective laser melting through inline coherent imaging *J. Mater. Process. Technol.* **231** 488–500

[5] Bamberg J, Spies M, Dillhöfer A, Rieder H and Hess T 2014 Online monitoring of additive manufacturing processes using ultrasound *Proc. of the 11th European Conf. on NonDestructive Testing* pp 6–10

[6] Gorden M, Zhang K and Collette M 2018 The strain amplification sensor: a 3D-printable stand-alone strain gauge for low-cost monitoring *Struct. Control Health Monit.* e2145

[7] Kleszczynski S, Zur Jacobsmühlen J, Reinarz B, Sehrt J T, Witt G and Merhof D 2014 Improving process stability of laser beam melting systems *Proc. of the Frauenhofer Direct Digital Manufacturing Conf.*

[8] Kleszczynski S, Zur Jacobsmühlen J, Sehrt J T and Witt G 2012 Error detection in laser beam melting systems by high resolution imaging *Proc. of the Solid Freeform Fabrication Symp.*

[9] Chakraborty P, Zhao G and Zhou C 2018 Unprecedented sensing of interlayer defects in three-dimensionally printed polymer by capacitance measurement *Smart Mater. Struct.* **27** 115012

[10] Chakraborty P, Gundrati N B, Zhou C and Chung D D L 2017 Effect of stress on the capacitance and electric permittivity of three-dimensionally printed polymer, with relevance to capacitance-based stress monitoring *Sensors Actuators* A **263C** 380–5

[11] Makagonov N G, Blinova E M and Bezukladnikov I I 2017 Development of visual inspection systems for 3D printing *2017 IEEE Conf. of Russian Young Researchers in Electrical and Electronic Engineering (EIConRus)* (https://doi.org/10.1109/EIConRus.2017.7910849)

[12] Li Y, Li Y F, Wang Q L, Xu D and Tan M 2010 Measurement and defect detection of the weld bead based on online vision inspection *IEEE Trans. Instrum. Meas.* **59** 1841–9

[13] Craeghs T, Clijsters S, Yasa E and Kruth J-P 2011 Online quality control of selective laser melting *Proc. of the Solid Freeform Fabrication Symp. (SFF) 2011*

[14] Hellstein P and Szwedo M 2016 3D thermography in non-destructive testing of composite structures *Meas. Sci. Technol.* **27** 124006

[15] Straub J 2015 Initial work on the characterization of additive manufacturing (3D printing) using software image analysis *Machines* **3** 55–71

[16] Okarma K and Fastowicz J 2016 No-reference quality assessment of 3D prints based on the GLCM analysis *2016 21st Int. Conf. on Methods and Models in Automation and Robotics (MMAR)* (https://doi.org/10.1109/MMAR.2016.7575237)

[17] Zur Jacobsmühlen J Z, Kleszczynski S, Schneider D and Witt G 2013 High resolution imaging for inspection of laser beam melting systems *Proc. of the 2013 IEEE Int. on Instrumentation and Measurement Technology Conf. (I2MTC) (Minneapolis, MN, 6–9 May 2013)* pp 707–12

[18] Erler M, Streek A, Schulze C and Exner H 2014 Novel machine and measurement concept for micro machining by selective laser sintering *Proc. of the Int. Solid Freeform Fabrication Symp. (Austin, TX, 4–6 August 2014)*

[19] Du S-C, Huang D-L and Wang H 2015 An adaptive support vector machine-based workpiece surface classification system using high-definition metrology *IEEE Trans. Instrum. Meas.* **64** 2590–604

[20] Neef A, Seyda V, Herzog D, Emmelmann C, Schönleber M and Kogel-Hollacher M 2014 Low coherence interferometry in selective laser melting *Phys. Procedia* **56** 82–9

[21] Holzmond O and Li X 2017 *In situ* real time defect detection of 3D printed parts *Addit. Manuf.* **17** 135–42

[22] Villarraga H, Lee C, Corbett T, Tarbutton J A and Smith S T 2015 Assessing additive manufacturing processes with x-ray CT metrology *Proc. ASPE 2015 Spring Topical Meeting: Achieving Precision Tolerances in Additive Manufacturing* pp 116–21

[23] Thompson A, Maskery I and Leach R K 2016 X-ray computed tomography for additive manufacturing: a review *Meas. Sci. Technol.* **27** 072001

[24] Warnett J M and Titarenko V 2016 Towards in-process x-ray CT for dimensional metrology *Meas. Sci. Technol.* **27** 035401

[25] Zhang B, Ziegert J, Farahi F and Davies A 2016 *In situ* surface topography of laser powder bed fusion using fringe projection *Addit. Manuf.* **12** 100–7

[26] Li Z and Liu X 2018 *In situ* 3D monitoring of geometric signatures in the powder-bed-fusion additive manufacturing process via vision sensing methods *Sensors* **18** 1180

[27] Grasso M and Colosimo B M 2017 Process defects and *in situ* monitoring methods in metal powder bed fusion: a review *Meas. Sci. Technol.* **28** 044005

[28] Rusu R B, Blodow N and Beetz M 2009 Fast point feature histograms (FPFH) for 3D registration *Proc. of the IEEE Int. Conf. on Robotics and Automation (ICRA)* (*Kobe, Japan*, *12–17 May 2009*) pp 3212–7

[29] Xinhua L, Shengpeng L, Zhou L, Xianhua Z, Xiaohu C and Zhongbin W 2015 An investigation on distortion of PLA thin-plate part in the FDM process *Int. J. Adv. Manuf. Technol.* **79** 1117–26

[30] Zhang Y and Chou Y K 2006 Three-dimensional finite element analysis simulations of the fused deposition modelling process *Proc. Inst. Mech. Eng.* B **220** 1663–71

[31] Levin D 2004 Mesh-independent surface interpolation *Geometric Modeling for Scientific Visualization* ed G Farin (Berlin: Springer) pp 37–49

[32] Papon J, Abramov A, Schoeler M and Worgotter F 2013 Voxel cloud connectivity segmentation—supervoxels for point clouds *The IEEE Conf. on Computer Vision and Pattern Recognition (CVPR)* pp 2027–34

[33] Jin H, Yezzi A J and Soatto S 2004 Region-based segmentation on evolving surfaces with application to 3d reconstruction of shape and piecewise constant radiance *Computer Vision—ECCV 2004* (Berlin: Springer) pp 114–25